Monthly Notices of the ROYAL ASTRONOMICAL SOCIETY

MNRAS **522,** 2516–2524 (2023) https://doi.org/10.1093/mnras/stad1102
Advance Access publication 2023 April 18

Optimizing the observation of optical kilonovae with medium-size telescopes

A. E. Camisasca [1★] I. A. Steele,[2] M. Bulla [1,3,4] C. Guidorzi [1,3,5] and M. Shrestha[2,6]

[1]*Department of Physics and Earth Science, University of Ferrara, via Saragat 1, I-44122 Ferrara, Italy*
[2]*Astrophysics Research Institute, Liverpool John Moores University, Liverpool Science Park IC2, 146 Brownlow Hill, Liverpool L3 5RF, UK*
[3]*INFN – Sezione di Ferrara, via Saragat 1, I-44122 Ferrara, Italy*
[4]*INAF – Osservatorio Astronomico d'Abruzzo, via Mentore Maggini snc, I-64100 Teramo, Italy*
[5]*INAF – Osservatorio di Astrofisica e Scienza dello Spazio di Bologna, via Piero Gobetti 101, I-40129 Bologna, Italy*
[6]*Steward Observatory, University of Arizona, 933 North Cherry Avenue, Tucson, AZ 85721-0065, USA*

Accepted 2023 April 11. Received 2023 April 3; in original form 2022 November 18

ABSTRACT

We consider the optimization of the observing strategy (cadence, exposure time, and filter choice) using medium-size (2-m-class) optical telescopes in the follow-up of kilonovae localized with arcminute accuracy to be able to distinguish among various kilonova models and viewing angles. To develop an efficient observation plan, we made use of the synthetic light curves obtained with the Monte Carlo radiative transfer code POlarization Spectral Synthesis In Supernovae for different kilonova models and as a function of different viewing angles and distances. By adding the appropriate photon counting noise to the synthetic light curves, we analysed four alternative sequences having the same total time exposure of 8 h, with different time windows (0.5, 1, 2, and 4 h), each with *i*, *r*, and *u* filters, to determine the observing sequence that maximizes the chance of a correct identification of the model parameters. We suggest to avoid *u* filter and to avoid the use of colour curves. We also found that, if the error on distance is $\leq$2 per cent, 0.5, 1, and 2-h time window sequences are equivalent, so we suggest to use 2-h one, because it has 1-d cadence, so it can be easily realized. When the distance of the source is unknown, 0.5-h time window sequence is preferable.

Key words: telescopes – black hole - neutron star mergers – gamma-ray bursts – neutron star mergers.

1 INTRODUCTION

Coalescences of neutron star binaries and black hole–neutron star systems lead to the formation of neutron-rich material. Such material undergoes rapid neutron capture nucleosynthesis (r-process) as it decompresses in space, leading to the creation of rare heavy elements such as gold and platinum (Li & Paczyński 1998). The radioactive decay of these unstable nuclei fuels a thermal transient known as 'kilonova' (hereafter, KN; see Metzger 2019 for a review). On 2017 August 17, Advanced LIGO/Virgo made the first detection (Abbott et al. 2017b) of gravitational waves (GWs) from a binary neutron star merger, GW170817, simultaneously with the detection of short gamma-ray burst (GRB) by *Fermi* (Goldstein et al. 2017) and *INTEGRAL* (Savchenko et al. 2017): GRB 170817A. 11 h after the GW170817 trigger, an optical counterpart was discovered in the nearby ($d = 40$ Mpc) galaxy NGC 4993 (Coulter et al. 2017). The ultraviolet, optical, and near-infrared emissions were consistent with being powered by the radioactive decay of nuclei synthesized in the merger ejecta by the r-process (Villar et al. 2017; Watson et al. 2019; Domoto et al. 2021; Kasliwal et al. 2022). This was the first time one source was detected both in GWs and electromagnetic (EM) radiation, and the first time spectroscopic evidence of a KN was obtained (Chornock et al. 2017; Kasen et al. 2017; Pian et al. 2017; Smartt et al. 2017).

The study of a KN's rapid evolution can improve our understanding of the role of neutron star mergers in the origin of heavy elements. In addition, KN spectra encode key information to constrain the outflows that produced their EM emission. There has been only one confirmed case of KN detection in the form AT2017gfo and few other possible candidates such as KNe associated to GRB 130603B (Tanvir et al. 2017) and GRB 211211A (Rastinejad et al. 2022). Hence, the whole community is working on various simulations to model the KN emission properties. There is a variety of predicted light-curve (LC) features (e.g. Wollaeger et al. 2018; Bulla 2019). Klion et al. (2021) and Nativi et al. (2021) showed how the presence of a jet impacts the KN LCs and makes them brighter and bluer when viewed pole on. Thus, it is important to come up with efficient observational strategies to get the best observational data to constrain the properties from computational models.

In this work, we aim to optimize the observing strategy for the optical follow-up of KNe to constrain the properties of the KN emission (viewing angle, mass of the different ejecta components, and their velocities), once this has been identified and localized with arcminute accuracy, which enables observations with narrow field facilities. Arcminute accuracy can be achieved with current high-energy instruments, such as the Burst Alert Telescope (Barthelmy et al. 2005) on board the *Neil Gehrels Swift Observatory* (Gehrels et al. 2004), or, in the near future, with *Space-based multi-band astronomical Variable Objects Monitor (SVOM*, Atteia, Cordier & Wei 2022), Einstein Probe (Yuan et al. 2022), and in the next decade possibly *Transient High-Energy Sky and Early Universe Surveyor*

★ E-mail: annaelisa.camisasca@unife.it

(THESEUS, Amati et al. 2021). Also, the advent of third-generation GW observatories, such as the Einstein Telescope (Punturo et al. 2010) and Cosmic Explorer (Abbott et al. 2017a), will lead to an accuracy in localization better than 10 deg^2 at $z < 3$, which is enough to enable prompt and efficient multiwavelength search for EM counterparts (Ronchini et al. 2022). A GW detector capable of arcminute accuracy or better could be realized within the Voyage 2050 programme (Baker et al. 2021).

We made extensive use of simulated multifilter LCs of KNe obtained with the POlarization Spectral Synthesis In Supernovae (POSSIS; Bulla 2019) code. Similar works recently carried out (e.g. Scolnic et al. 2018; Setzer et al. 2019; Almualla et al. 2021; Andreoni et al. 2022; Chase et al. 2022; Colombo et al. 2022) focus on optimizing strategies of wide field and follow-up facilities to detect KNe. In this work, instead, we aim to determine the optimal combinations of time exposure sequence and filters that help to constrain the model parameters with follow-up instruments.

We chose to study the specific case of small–medium-class instruments; we considered two optical imaging cameras that are currently deployed at the 2-m fully robotic Liverpool Telescope (Steele et al. 2004): Multicolour OPTimised Optical Polarimeter (MOPTOP, Shrestha et al. 2020) and IO:O (Smith & Steele 2017). We assume that a network of similar telescopes and instruments (e.g. Tsapras et al. 2009) is located throughout a range of longitudes such that 24-h coverage is available. Given the interest in such sources, this assumption is reasonable in that most telescopes worldwide are likely to be involved in the follow-up of such rare events (e.g. Brown et al. 2013).

In Section 2, we describe the characteristics of KN models generated with POSSIS. In Sections 3 and 4, we describe, respectively, the preliminary procedure and results obtained under the hypothesis of known source distance. In Sections 5 and 6, we introduce the procedure and the results we adopted under the assumption of a distance uncertainty. We report our conclusions in Section 7.

2 MODEL PARAMETERS

We use KN models produced with POSSIS, a 3D Monte Carlo radiative transfer code that predicts photometric and polarimetric signatures of supernovae and KNe (Bulla 2019). The modelled ejecta are taken from Nativi et al. (2021), where a neutrino-driven wind as described in Perego et al. (2014) was evolved assuming that either no jet (`Wind`), or a jet with a luminosity of $L_j = 10^{49}$ erg s^{-1} (`Jet49`), or a jet with $L_j = 10^{51}$ erg s^{-1} (`Jet51`) is launched. The wind mass is dominated by a secular component ejected 1 s after the merger with 0.072 $M_\odot$. Unlike in Nativi et al. (2021), here we include an additional component to model dynamical ejecta. Specifically, we adopt an idealized geometry for this component, with a lanthanide-rich dynamical ejecta component ($Y_e = 0.15$ and velocities from 0.08 to 0.3c) from the grid in Dietrich et al. (2020) and selecting the best-fitting model to the KN of GW170817 (mass 0.005 $M_\odot$ and half-opening angle of 30°). These models are referred to as `Wind-dyn`, `Jet49-dyn`, and `Jet51-dyn` to distinguish them from those in Nativi et al. (2021). Fig. 1 shows density and Y_e distributions for the three models.

Radiative transfer simulations are carried out for the three models using the latest version of POSSIS (Bulla 2023). Compared with the first version of the code (Bulla 2019, also used by Nativi et al. 2021), the improved version assumes heating rates (Rosswog & Korobkin 2022), thermalization efficiencies (Barnes et al. 2016; Wollaeger et al. 2018), and wavelength- and time-dependent opacities (Tanaka et al. 2020) that depend on the local properties of the ejecta such as density, temperature, and electron fraction. For each of the three models, we extract KN LCs for 11 different inclination angles for each model. Consequently, for a given distance and filter one has 33 different LCs. LCs are computed by POSSIS from 0.1 to 30 d after the merger, but for this work we focus on the time window from 1.0 to 5.0 d after the merger. We decided to ignore the code predictions earlier than 1 d after the merger because current opacity values assumed by POSSIS are likely affected by inaccuracies in the presence of highly ionized ejecta (Tanaka et al. 2020). We do not consider LCs after 5 d due to the low value of flux.

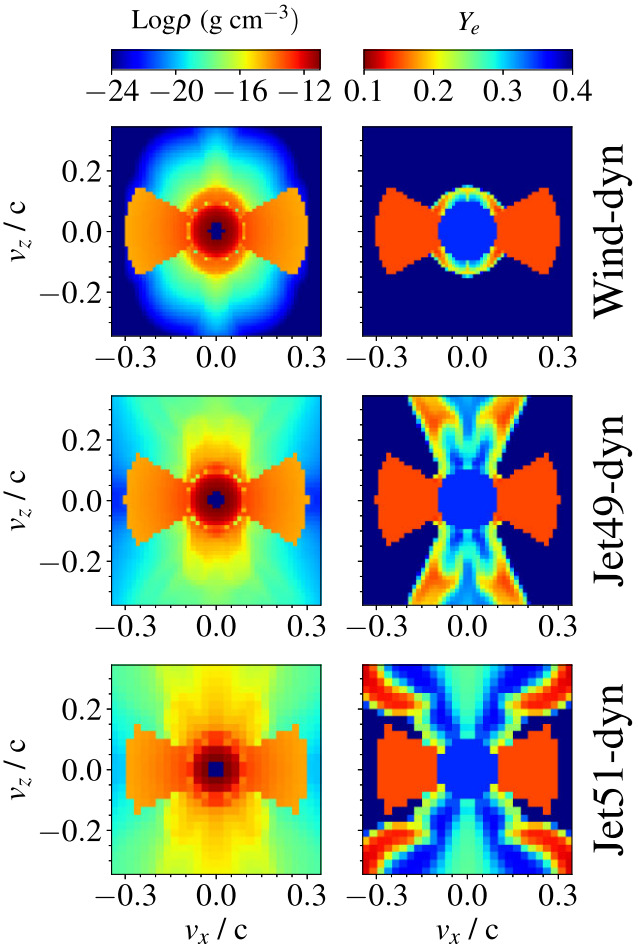

Figure 1. Density (left) and Y_e (right) distribution in the x−z plane for the three models used in this study (`Wind-dyn`, `Jet49-dyn`, and `Jet51-dyn` from top to bottom). Density maps are shown at 1 d after the merger.

The viewing angle θ is defined as the angle between the direction perpendicular to the merging plane and the line of sight. We used 11 values for the viewing angle separated by a constant step in cosine of 0.1: $\cos\theta$ can assume the values 0, 0.1, 0.2, ..., 1, with $\cos\theta = 0$ corresponding to an observer in the merger plane (edge-on view) and $\cos\theta = 1$ to an observer along the jet axis (face-on view). We assumed the following range of values for distance: 20, 40, 80, 160, 250, and 350 Mpc.

We chose to evaluate our results considering observations in the Sloan filters i', r', and u' (hereafter referred to as i, r, and u). These wavebands were chosen as being commonly available at most telescopes. In particular, we were keen to understand what (if any) additional value was added by carrying out u-band observations, which are generally seen as more difficult than the r and i bands

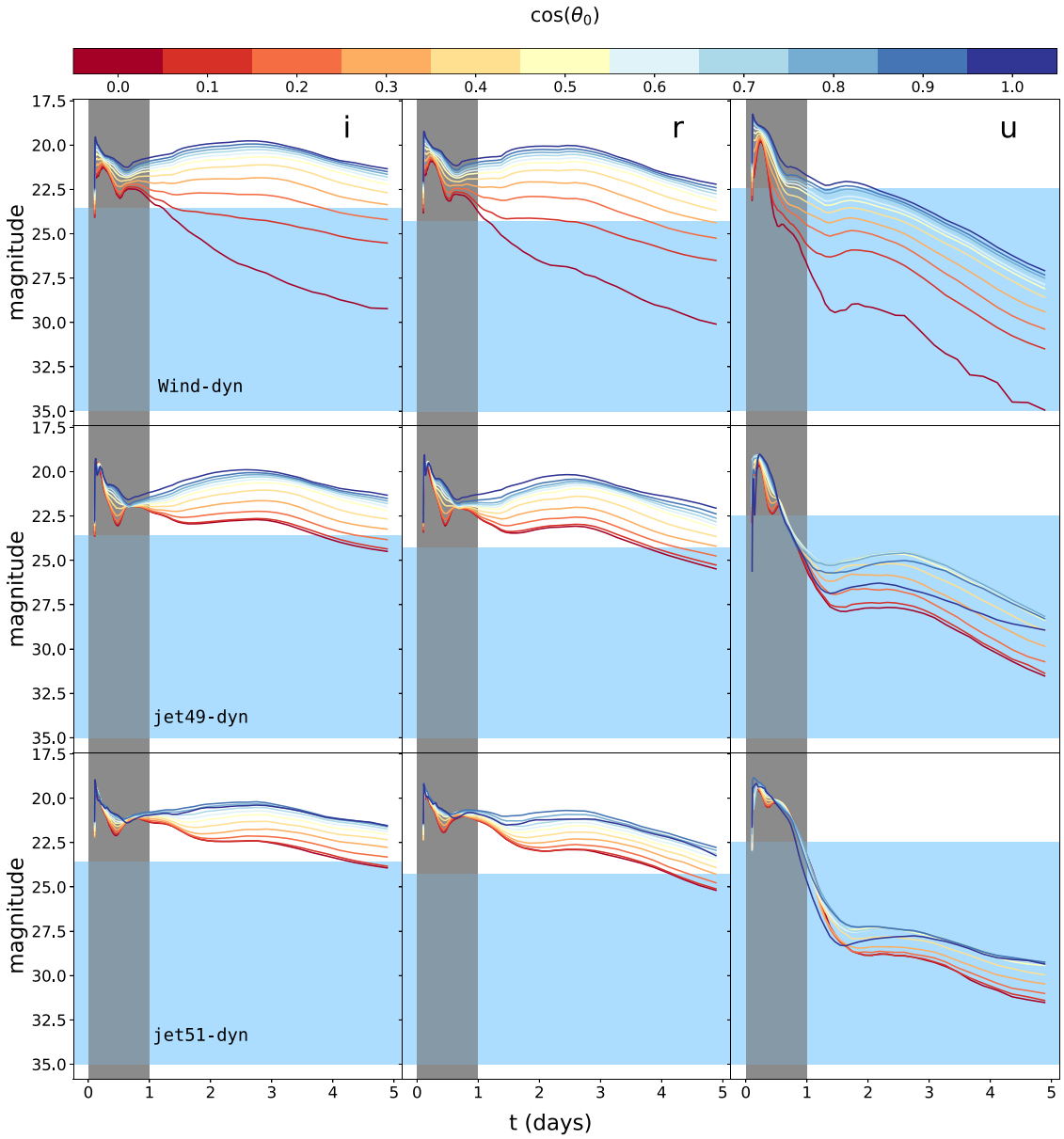

Figure 2. LCs for different models and viewing angles; first column refers to filter *i*, second one to filter *r*, and third to filter *u*; the source has a distance of 160 Mpc. Grey area corresponds to the first day after the merger: LCs are not considered due to the inaccuracy in estimating the opacity. The blue area corresponds to the values in magnitude higher than the limiting magnitude of each filter, obtained with a time exposure of 1 h.

due to lower system throughputs and detector quantum efficiencies at near-ultraviolet wavelengths.

In Fig. 2, we show the LCs obtained with $d = 160$ Mpc for different filters, models, and viewing angles. The KN brightness decreases going from the jet axis ($\cos\theta = 1$) to the merger plane ($\cos\theta = 0$) for all the three models, an effect that is caused by the presence of lanthanide-rich dynamical ejecta material absorbing part of the escaping flux ('lanthanide curtain'; Kasen, Fernández & Metzger 2015; Wollaeger et al. 2018). The area highlighted in light blue in Fig. 2 shows, for each filter, the magnitudes that are not detectable. Limiting magnitudes were obtained imposing a minimum signal-to-noise ratio (SNR) threshold of 5. See Appendix A for more details.

We point out that our study is restricted to a specific configuration in terms of ejecta properties (e.g. masses and compositions), since we do not aim to assess the ability of medium-size telescopes to constrain these properties, but rather to select the correct model and correct viewing angle. Extending this analysis to a large grid of models with different ejecta properties is beyond the scope of this paper and could be done in the future.

3 PROCEDURE WITH KNOWN DISTANCES

In order to find a reasonable time exposure sequence necessary to distinguish between different KN models characterized by different viewing angles, we follow three main steps:

(i) We considered four different time exposure sequences, see Section 3.1 for a detailed explanation.

(ii) For a fixed distance and filter, we add the appropriate photon counting noise to the LC; the results depend on the time exposure

Table 1. Duration of time exposure windows and cadence for four different time exposure sequences.

Name	Duration Time exposure window (h)	Cadence (d)
A	0.5	0.25
B	1	0.5
C	2	1
D	4	See Section 3.1 for a description

sequence; we apply this step to all 33 LCs. Henceforward we will call the LC with noise 'LCN' (see Section 3.2).

(iii) We compare LCN with the LCs without noise and we analyse how often we are able to identify the correct LC. This is done for each combination of distance and filter. We repeat this for all the 33 different LCNs (see Section 3.3).

In the first part, the distance of the source is assumed to be known with negligible uncertainty, so we compare LCNs with LCs at the same distance.

3.1 Time exposure sequences

We considered four different time exposure sequences (hereafter, referred to as A, B, C, and D), each of them with a total net exposure of 8 h. Table 1 reports the time windows and cadence for A, B, and C sequences. Sequence D requires a separate description: it consists of two 4-h intervals 1 d apart. The exact times of the two observations are determined by maximizing the difference between the two expected magnitude values taking into account the corresponding uncertainties. To this aim, for each instant we find the median of

$$\frac{|m_{\mathrm{model}_i} - \overline{m}|}{\sigma_{m_i}}, \tag{1}$$

where m_{model_i} is the magnitude of the ith LC at that instant, $\overline{m}$ is the mean of all 33 LCs at that instant, and σ_{m_i} is

$$\sigma_{m_i} = \frac{1}{0.4\sqrt{F_i t_{\mathrm{exp}}}\ln(10)},$$

where F_i is the photoelectron count expected in 1 s for the ith model and $t_{\mathrm{exp}} = 4$ h. We sum the median (equation 1) obtained with different filters and distances and we find the mean value of this quantity in 4-h intervals. We finally determine the maximum of the sum of the value obtained in two 4-h intervals 1 d apart. In this way, we obtain the intervals where the models are more different. Fig. 3 displays the resulting time windows.

3.2 Adding noise to light curves

We used A, B, C, and D time exposure sequences to simulate different LCNs for all combinations of filters, distances, viewing angles, and models. In more detail, at each time we calculated the expected photoelectron counts as $t_{\mathrm{exp}}(F + F_{\mathrm{sky}})$, where F_{sky} are the counts s^{-1} due to the sky (see Appendix A for more details). We then obtained the simulated counts C_{P} by adding the statistical noise assuming the Poisson distribution.

The noise-affected flux of the kth LC is calculated as follows:

$$F_{\mathrm{noise},k} = \frac{C_{\mathrm{P},k}}{t_{\mathrm{exp}}} - F_{\mathrm{sky}}, \tag{2}$$

along with the corresponding magnitude

$$m_{\mathrm{noise},k} = z_{\mathrm{P}} - 2.5\,\log_{10}(F_{\mathrm{noise},k})\,. \tag{3}$$

Equation (3) gives a generic LCN. Fig. 3 shows the results of this step.

3.3 Comparison between LC with noise and models

We compare any given LCN with all of the 33 models and select the model that minimizes the following χ^2:

$$\chi^2(k,i) = \sum_{j=0}^{N_t}\left(\frac{m_{\mathrm{model}_i}(t_j) - m_{\mathrm{noise}_k}(t_j)}{\sigma_{m_{\mathrm{noise}_k}}(t_j)}\right)^2 \cdot \frac{1}{N_t}, \tag{4}$$

where we are summing over the N_t different data, i and k, respectively, identify LC and LCN, and $\sigma_{m_{\mathrm{noise},k}}$ is the uncertainty on $m_{\mathrm{noise},k}$, obtained by error propagating from $C_{\mathrm{P},k}$, using equations (2) and (3) and assuming $\sigma_{C_{\mathrm{P},k}} = \sqrt{C_{\mathrm{P},k}}$. It is given by

$$\sigma_{m_{\mathrm{noise},k}} = \frac{\sqrt{C_{\mathrm{P},k}}}{0.4F_{\mathrm{noise},k}\ln(10)t_{\mathrm{exp}}}. \tag{5}$$

In this way, we obtain, for each model, viewing angle and distance (so, for each configuration), using four different time exposure sequences, the number of correct/incorrect matches.

4 RESULTS WITH KNOWN DISTANCES

Fig. 4 shows, for each distance and for each model, the number of incorrect matches out of 33 comparisons. Noticeably, it is better to avoid u filter. Hereafter, in our analysis, we will consider only i and r filters.

We take note of three different kinds of mismatching errors between the simulated data points and the model LC:

(i) The most similar curve model corresponds to the simulated model, but the viewing angle is wrong.
(ii) The most similar model turns out to be different from the original one.
(iii) LCN is not detectable because the magnitude value is higher than the limiting value for each point of LCN.

We summarize the results about the most common mismatches (i.e. misidentifications) in the left-hand pie of Fig. 5. The outermost ring corresponds to the different number of mismatches obtained with the four exposure combinations (i and r filters); the innermost one refers to the different kinds of mismatches. Overall, most of the mismatches are of type (iii). The percentage of mismatches of type (ii) is higher than that of type (i). Type (ii) mismatches are shown in the central pie of Fig. 5 including both i and r filters; undetectable LCs are ignored. The number of mismatches is quite similar among all the kinds of models and with every sequence. If we consider i and r filters individually, the results are similar; if we include the not detectable LCs, the number of mismatches with `Wind-dyn` model increases. Let θ_0 be the viewing angle of the LCN. We check if there is any particular value of θ_0 for which we have most of the mismatches and how significant the mismatch is for the different viewing angle θ_0. As shown in the right-hand pie of Fig. 5, D time exposure sequence has a wider range of starting angle that can bring to mismatches; with A, B, and C most mismatches happen for $78^\circ \leq \theta_0 \leq 90^\circ$. Analysing the difference between $\cos\theta_0$ and the value of $\cos\theta$ of the most similar LC, we find that with C time exposure sequence we always have $|\Delta\cos\theta| \leq 0.1$; with A and B we have more than 80 per cent of mismatches with $|\Delta\cos\theta| \leq 0.2$, with D it is 62 per cent.

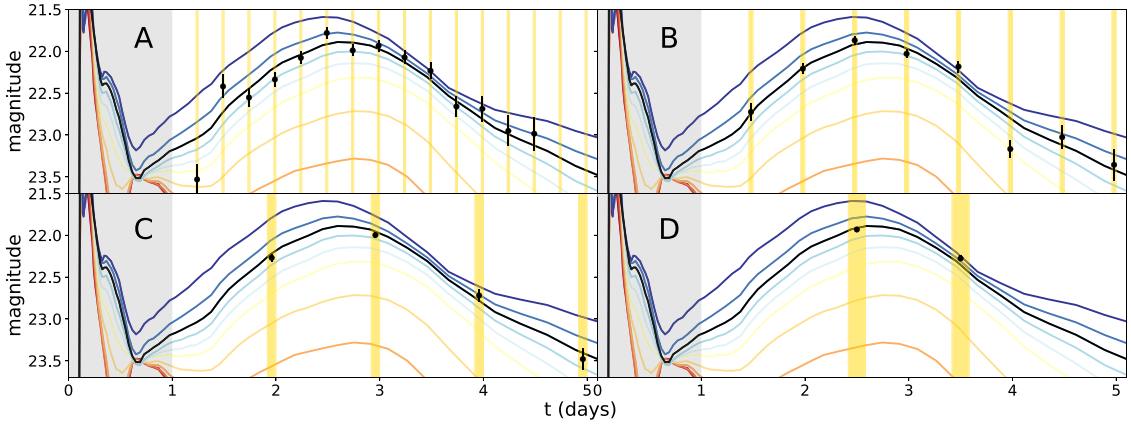

Figure 3. Each panel refers to a different time window sequence: A, B, C, and D. In yellow, A, B, C, and D time windows; in each plot, LCs referring to `Jet49-dyn` model, $d = 350$ Mpc, and *i* filter. Black lines are LCs with $\cos\theta_0 = 0.8$, black points refer to the corresponding LCNs.

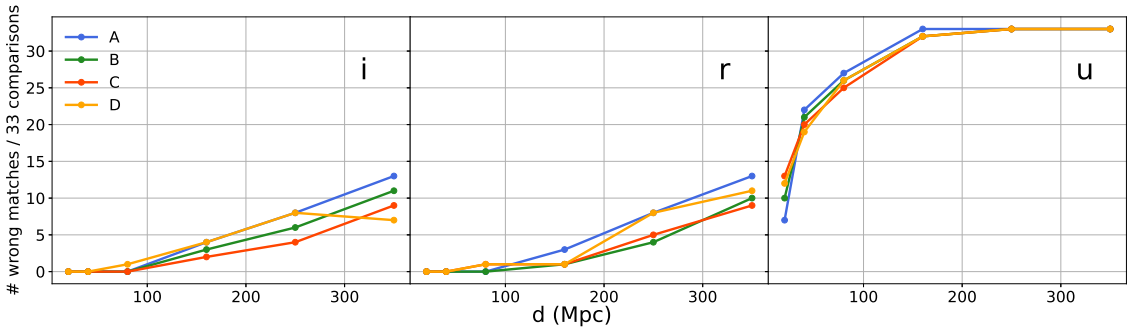

Figure 4. Number of wrong matches as a function of distance for different filters and different time exposure sequences.

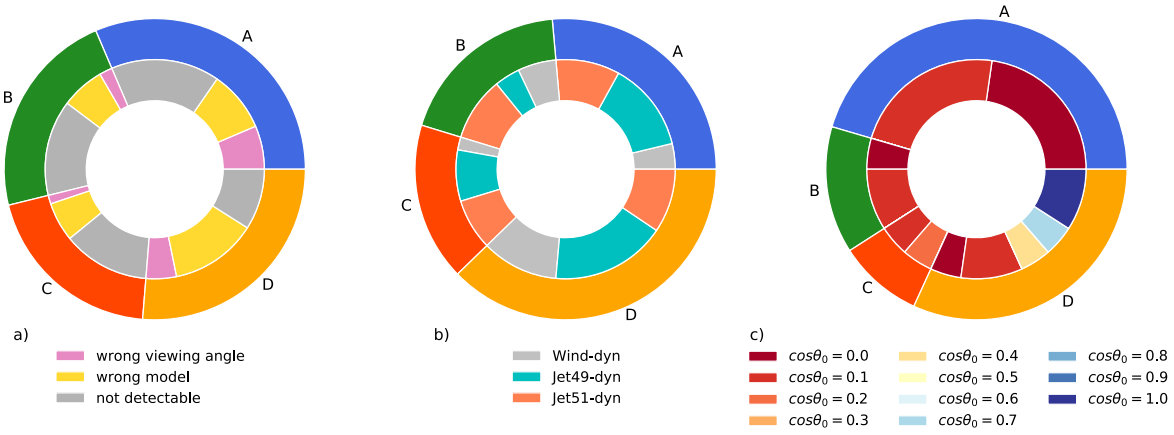

Figure 5. For every different time exposure sequence, we analyse the type of mismatch that occurs in comparing the simulated curve with the model ones. We considered both *i* and *r* filters. (a) In the outer ring, the number of wrong matches for each time exposure; in the inner ring, the kind of mismatch. (b) For every different time exposure sequence, we analyse which model is more difficult to detect. In the outer ring, the number of wrong matches for each time exposure; in the inner ring, the number of mismatch for each kind of model. (c) In the outer ring, the number of wrong matches for each time exposure; in the inner ring, $\cos\theta_0$.

The fact that the most of the mismatches refer to edge-on view and that *i* and *r* filters perform better than *u* can easily be understood looking at Fig. 2:

(i) Edge-on-view LCs are more significantly affected by statistical noise, since they have lower fluxes than face-on ones; also, they can partially or totally fade below the limiting magnitude to the point that they become undetectable.

(ii) *u*-filter LCs have lower fluxes and their limiting magnitude value is lower than *i* and *r* ones; these characteristics lead to a low performance of the *u* filter.

5 PROCEDURE WITH DISTANCE UNCERTAINTY

We now examine the realistic situation of non-negligible uncertainty on distance, and, in addition, the possibility that there is no information on the distance of the source as well as on the time of the merger. We restrict our analysis to *i* and *r* filters, due to the low performance of *u*.

5.1 1 and 2 per cent error on distance

We analysed the consequences of an error on distance of 1 and 2 per cent. Such a level of accuracy in estimating the distance based on GW data alone appears to be feasible for a sizeable fraction of cases: third-generation GW detector network will measure distances with an accuracy of 0.1–3 per cent for sources within $\leq$300 Mpc (see fig. 9 from Gupta et al. 2019). To study this case, when we look for the matches between LCN and LCs, we shift the magnitude of the LC models due to the error on distance. We consider both a +1 per cent (+2 per cent) and −1 per cent (−2 per cent) error on distance.

5.2 Unknown distance, χ^2-minimization technique

Let us assume that we have no information on distance as well as on the merger time. When we have to compare LCN with LCs, we start using the LCs model with the intermediate distance of 160 Mpc (LC-160) and we shift LC-160 both in time (Δt) and in magnitude (Δm), in order to find, among the 33 comparisons, Δt and Δm that minimize χ^2 (equation 4). Once we have Δm, we follow this procedure:

(i) We use Δm to find an estimated distance (d_s) of the source.
(ii) We create a set of LC models with which to compare LCN, with a step of 0.1 mag between one model and the following one.
(iii) We choose the model with the nearest distance to d_s.
(iv) We compare LCN with the model at the most similar distance with d_s, shifting LCs both in time and magnitude to find the best match.

5.3 Colour curves technique

We adopted colour curves to try to limit the possible effect of distance uncertainties. To create colour curve with noise (CCN), we add noise to LCs with different filters, then we subtract them. Since CCNs have a dependence on distance (even if small), when we compare CCNs with colour curve models (CCs), we compare them with CCs model at the intermediate distance of 160 Mpc (CC-160).

6 RESULTS WITH DISTANCE UNCERTAINTY

6.1 Single filter technique

In Fig. 6, we present the number of wrong matches that occur in 33 comparisons with A, B, C, and D time exposure sequences, using filters individually. We reported the results obtained without error on distance and we compare it with what we obtain with an error of 1 per cent, 2 per cent, and without information on distance and time of the merger. For 1 per cent (and 2 per cent) error on distance, we plot the highest number of mismatches between +1 and −1 per cent (+2 and −2 per cent).

For each filter, each distance, we compare the results obtained with A, B, C, and D checking if the number of mismatches within each time exposure sequence is compatible with the best results obtained within the limits of Poisson statistics.[1] In Fig. 6, we marked with 'x' the cases that are significantly different from the best value obtained with other time sequences; if the error on distance is $\leq$2 per cent, no particular statistical differences emerge between sequences A, B, and C. When the distance is unknown, C and D time windows should be avoided. Hereafter, we restrict our analysis to A and C time exposure sequences, since C, with 1-d cadence, can easily be carried out with a single telescope, but should be avoided when no information on the source distance is available. The comparison between *i* and *r* shows that they are equivalent.

6.1.1 *Error on distance* $\leq$2 per cent

Focusing on time sequence C with error on distance $\leq$2 per cent, Fig. 7 shows that the number of mismatches of types (i), (ii), and (iii) is mostly the same. The number of mismatches concerning the models are equally distributed between `Wind-dyn`, `Jet49-dyn`, and `Jet51-dyn`, provided that the LC can be detected. If we consider also not detectable LCNs, `Wind-dyn` model mismatches increase (i.e. `Wind-dyn` model would be harder to be detected). With an error on distance of 1 per cent, the majority of the mismatches are in the interval $73^\circ \leq \theta_0 \leq 90^\circ$; this interval becomes wider for increasing errors on distance. When the error on distance is $\leq$2 per cent, both with *i* and *r* filters we have $|\Delta\cos\theta| \leq 0.2$ for all the mismatches.

6.1.2 *Unknown distance*

If we do not have information about the distance, in order to have the lowest number of mismatches, it is recommendable to use A time window sequence; with this sequence the number of mismatches of types (i), (ii), and (iii) is similar; also, the mismatches concerning the models are equally distributed among `Wind-dyn`, `Jet49-dyn`, and `Jet51-dyn`. Regarding viewing angle mismatches, they occur with the same frequency for every θ_0; furthermore, $|\Delta\cos\theta| \leq 0.2$ for 82 per cent of mismatches.

6.1.3 *Focus on viewing angle estimation*

For each combination of distance and of its error, we adopted the following procedure: for each viewing angle θ_0, we determined the uncertainty on the estimated viewing angle θ_{est}, using either C or A time sequence, respectively, for error on distance $\leq$2 per cent and for unknown distance. Then, we took the largest uncertainty among all the values of θ_0: in this way, we associated to any combination of distance and error on it with a conservative uncertainty in the estimated viewing angle, as the result of any possible value of θ_0. Table 2 reports the results.

If the error on distance is $\leq$2 per cent, the error on θ_{est} is always $\leq 7^\circ$; these errors implicitly assume that the inaccuracies intrinsic to the POSSIS models and its assumptions are negligible. In practice,

[1]When we compare the results of two observations N_1 and N_2, we assume that the numbers of wrong matches are independently Poisson distributed. Consequently, $|N_2 - N_1|$ is the absolute value of a Skellam-distributed random variate. We calculate the probability of having $\geq|N_2 - N_1|$ assuming as expected value for the common Poisson distribution the mean value of N_1 and N_2. When the probability is <5 per cent, the two numbers are considered significantly different.

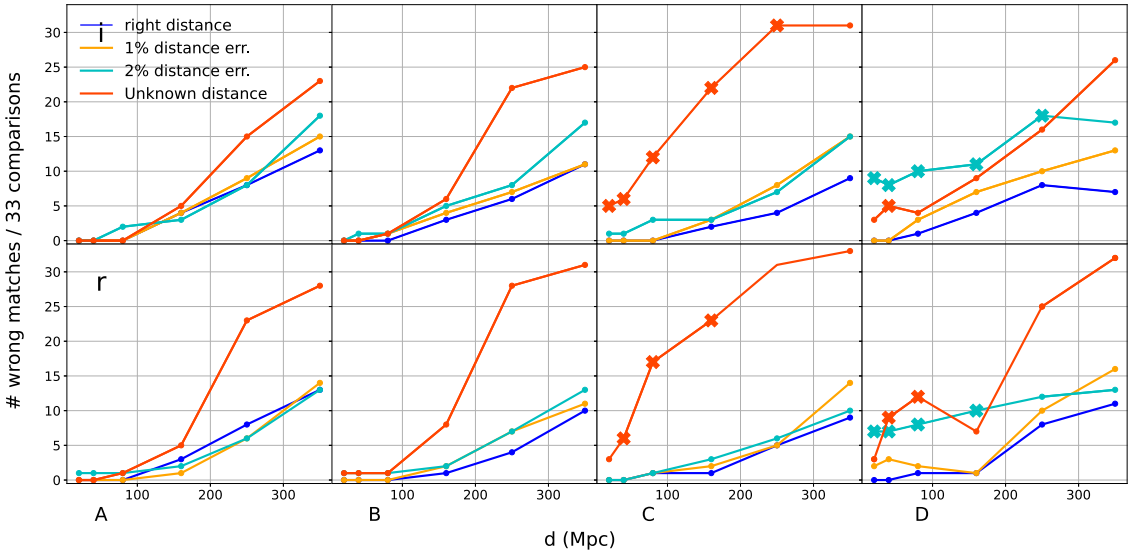

Figure 6. The number of wrong matches that occur in 33 comparisons with A, B, C, and D time exposure sequences with a known distance (blue line), with an error of 1 per cent on distance (yellow line), 2 per cent (cyan line), and without any information about the distance and the time of the merger (orange line). Points marked with 'x' refer to values that are significantly different from the best value obtained with other time sequences.

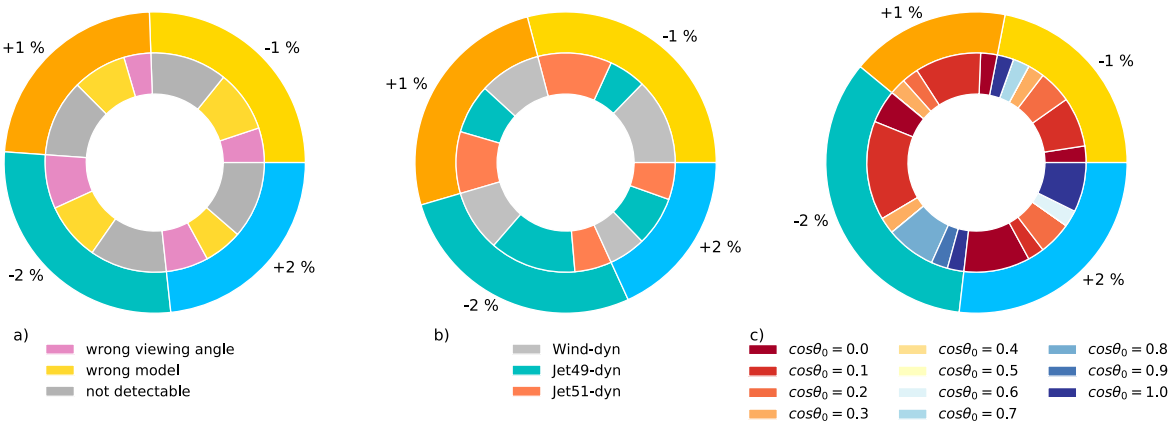

Figure 7. Using time sequence C, we consider the number of wrong matches we have when we make an error on distance of ±1 and ±2 per cent. (a) In the outer ring, the number of wrong matches for each error on distance; in the inner ring, the kind of mismatch. (b) For every different model of the simulated source, we analyse how many mismatches we have. (c) For every different observational direction, we analyse the number of mismatches.

Table 2. The higher standard deviation on θ_{est} for different distances.

d (Mpc)	1 per cent distance err.	2 per cent distance err.	Unknown distance
20	3°	4°	11°
40	2°	7°	7°
80	1°	4°	5°
160	3°	4°	12°
250	2°	4°	14°
350	7°	4°	25°

should this be no more the case; an independent estimate of the viewing angle, combined with the errors reported in Table 2, could help to constrain the POSSIS accuracy, thus providing useful feedback to tweak and refine the code itself.

6.2 Colour curve technique

For each time windows sequence, we analysed the results obtained comparing CCN with CC-160 for *i*–*r* CCs. As we can see in Fig. 8, this procedure gives a higher number of wrong matches than single filter techniques; this is due to the fact that the use of two LCs increases the possibility that, in a given instant, there is at least one undetectable LC. Moreover, uncertainties on both curves combine and lower the SNR; furthermore, LCs in *i* and *r* are really similar and there is really little viewing angle dependence in *i*–*r* colour. We do not consider *i*–*u* and *r*–*u* CCs due to *u*-filter outcomes; using another filter combined with *i* and r might lead to better results. Finally, since there is a slight dependence of CCs on distance, we use in the comparison CC-160; this makes the match more difficult when the distance is highly different from 160 Mpc.

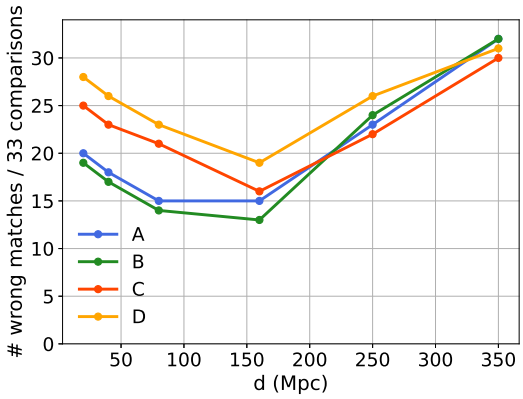

Figure 8. Number of wrong matches as a function of distance for different time exposure sequence using colour curves *i*–*r*.

7 CONCLUSIONS

The aim of the paper was finding the best strategy to characterize accurately localized KNe with follow-up small–medium-size optical telescopes. We found that the use of the *u* filter should be avoided, due to the high number of mismatches with all the time window sequences considered in this work (see Fig. 4). Even a procedure with *i*–*r* colour curve is not as convenient as one might think: it gives a higher number of wrong matches than single filter technique, due to the fact that the use of two LCs increases the possibility that, in a moment, there is at least one undetectable LC. Alternative time window sequences sharing the same total net exposure and with at least four observations and a maximum cadence of 1 d are essentially equivalent, provided that the error on distance is $\leq$2 per cent. Consequently, we suggest to use 1-d-cadence sequence, because it can be easily realized. If the distance of the source is unknown, short-cadence ($\leq$0.5 d) sequences are preferable.

Finally, we demonstrated that, for any distance considered in the present analysis (from 20 to 350 Mpc) and an error on distance $\leq$2 per cent, the viewing angle is estimated very accurately: the correct value is always compatible with the estimated one within uncertainties, with an error that is always $\leq 7^{\circ}$. This means that an independent measurement of the viewing angle could help to constrain the accuracy of POSSIS, providing useful information to refine the code itself. In addition, more stringent constraints on the viewing angle can better reduce the distance–inclination angle degeneracy in GW data, and, consequently, lead to a more accurate estimate of the distance and of the Hubble constant H_0 (e.g. Guidorzi et al. 2017; Dhawan et al. 2020; see Bulla et al. 2022 for a review).

ACKNOWLEDGEMENTS

We are grateful to the Referee for the careful reading and constructive comments, which helped us to improve the paper. AEC thanks IAS for the hospitality at the Astrophysics Research Institute of Liverpool JM University and the significant research opportunity and acknowledges the University of Ferrara for financial support under the programme 'Call for mobility scholarship for periods at European and extra European Institutions'. The radiative transfer simulations with POSSIS were performed on resources provided by the Swedish National Infrastructure for Computing (SNIC) at Kebnekaise.

DATA AVAILABILITY

The *uri* LCs for the six models used in this study will be made available at https://github.com/mbulla/kilonova_models. The POSSIS code used to simulate the LCs is not publicly available.

REFERENCES

Abbott B. P. et al., 2017a, Class. Quantum Gravity, 34, 044001
Abbott B. P. et al., 2017b, ApJ, 848, L12
Almualla M. et al., 2021, MNRAS, 504, 2822
Amati L. et al., 2021, Exp. Astron., 52, 183
Andreoni I. et al., 2022, ApJS, 260, 18
Atteia J. L., Cordier B., Wei J., 2022, Int. J. Mod. Phys. D, 31, 2230008
Baker J. et al., 2021, Exp. Astron., 51, 1441
Barnes J., Kasen D., Wu M.-R., Martínez-Pinedo G., 2016, ApJ, 829, 110
Barthelmy S. D. et al., 2005, Space Sci. Rev., 120, 143
Brown T. M. et al., 2013, PASP, 125, 1031
Bulla M., 2019, MNRAS, 489, 5037
Bulla M., 2023, MNRAS, 520, 2558
Bulla M., Coughlin M. W., Dhawan S., Dietrich T., 2022, Universe, 8, 289
Chase E. A. et al., 2022, ApJ, 927, 163
Chornock R. et al., 2017, ApJ, 848, L19
Colombo A., Salafia O. S., Gabrielli F., Ghirlanda G., Giacomazzo B., Perego A., Colpi M., 2022, ApJ, 937, 79
Coulter D. A. et al., 2017, Science, 358, 1556
Dhawan S., Bulla M., Goobar A., Sagués Carracedo A., Setzer C. N., 2020, ApJ, 888, 67
Dietrich T., Coughlin M. W., Pang P. T. H., Bulla M., Heinzel J., Issa L., Tews I., Antier S., 2020, Science, 370, 1450
Domoto N., Tanaka M., Wanajo S., Kawaguchi K., 2021, ApJ, 913, 26
Gehrels N. et al., 2004, ApJ, 611, 1005
Goldstein A. et al., 2017, ApJ, 848, L14
Guidorzi C. et al., 2017, ApJ, 851, L36
Gupta A., Fox D., Sathyaprakash B. S., Schutz B. F., 2019, ApJ, 886, 71
Kasen D., Fernández R., Metzger B. D., 2015, MNRAS, 450, 1777
Kasen D., Metzger B., Barnes J., Quataert E., Ramirez-Ruiz E., 2017, Nature, 551, 80
Kasliwal M. M. et al., 2022, MNRAS, 510, L7
Klion H., Duffell P. C., Kasen D., Quataert E., 2021, MNRAS, 502, 865
Li L.-X., Paczyński B., 1998, ApJ, 507, L59
Metzger B. D., 2019, Living Rev. Relativ., 23, 1
Nativi L., Bulla M., Rosswog S., Lundman C., Kowal G., Gizzi D., Lamb G. P., Perego A., 2021, MNRAS, 500, 1772
Perego A., Rosswog S., Cabezón R. M., Korobkin O., Käppeli R., Arcones A., Liebendörfer M., 2014, MNRAS, 443, 3134
Pian E. et al., 2017, Nature, 551, 67
Punturo M. et al., 2010, Class. Quantum Gravity, 27, 194002
Rastinejad J. C. et al., 2022, Nature, 612, 223
Ronchini S. et al., 2022, A&A, 665, A97
Rosswog S., Korobkin O., 2022, Annalen der Physik, Heavy Elements and Electromagnetic Transients from Neutron Star Mergers. Available at:
Savchenko V. et al., 2017, ApJ, 848, L15
Scolnic D. et al., 2018, ApJ, 852, L3
Setzer C. N., Biswas R., Peiris H. V., Rosswog S., Korobkin O., Wollaeger R. T., LSST Dark Energy Science Collaboration, 2019, MNRAS, 485, 4260
Shrestha M., Steele I. A., Piascik A. S., Jermak H., Smith R. J., Copperwheat C. M., 2020, MNRAS, 494, 4676
Smartt S. J. et al., 2017, Nature, 551, 75
Smith R., Steele I. A., 2017, Technical Report, Liverpool Telescope Technical Note 1: Telescope and IO:O Throughput
Steele I. A. et al., 2004, in Oschmann J. M. J.ed., Proc. SPIE Conf. Ser. Vol. 5489, Ground-based Telescopes. SPIE, Bellingham, p. 679
Tanaka M., Kato D., Gaigalas G., Kawaguchi K., 2020, MNRAS, 496, 1369
Tanvir N. R. et al., 2017, ApJ, 848, L27
Tsapras Y. et al., 2009, Astron. Nachr., 330, 4
Villar V. A. et al., 2017, ApJ, 851, L21

Watson D. et al., 2019, Nature, 574, 497
Wollaeger R. T. et al., 2018, MNRAS, 478, 3298
Yuan W., Zhang C., Chen Y., Ling Z., 2022, in Bambi C., Santangelo A., eds, Handbook of X-ray and Gamma-ray Astrophysics. Springer, Singapore

APPENDIX: EXPOSURE TIME FORMULA FOR A SINGLE FILTER

We calculate $F_{\rm lim}$, defined as the minimum photoelectron count collected in 1 s to have a detectable signal, assuming a limiting SNR, $\mathrm{SNR}_{\rm lim} = 5$, through the following equation:

$$\mathrm{SNR}_{\rm lim} = \frac{F_{\rm lim}\, t_{\rm exp}}{\sqrt{F_{\rm lim} t_{\rm exp} + F_{\rm sky} t_{\rm exp}}},$$

with

$$F_{\rm sky} = 10^{0.4(z_{\rm P} - m_{\rm sky})}\, A,$$

where $z_{\rm P}$ is the instrument zero-point referred to a particular filter (the magnitude corresponding to one detected photoelectron per second), $m_{\rm sky}$ is the sky magnitude in 1 arcsec^2, and A is the area of the photometric aperture used. We used $z_{\rm P}$ and $m_{\rm sky}$ values as suggested at the Liverpool Telescope website,[2] assuming $m_{\rm sky}$ as intermediate between a dark and a bright sky (Table A1). Since the typical La Palma seeing is 0.75 arcsec, we adopted an aperture diameter two times that value (i.e. 1.5 arcsec), which yields $A = 1.8$ arcsec^2.

Table A1. $z_{\rm P}$ and $m_{\rm sky}$ values.

Filter	$z_{\rm p}$	$m_{\rm sky}$ (mag arcsec^{-2})
i	25.06	17.3
r	15.39	18.4
u	21.00	18.0

[2] https://github.com/LivTel/ETC_calcs/blob/master/NRT_calc.html

This paper has been typeset from a TEX/LATEX file prepared by the author.